Broadband spectral responses in visual cortex revealed by a new MEG denoising algorithm

Eline R. Kupers[1], Helena X. Wang[1], Kaoru Amano[2], Kendrick N. Kay[3], David J. Heeger[1], Jonathan Winawer[1]

Author institutions

1. Department of Psychology and Center for Neural Science, New York University
2. Center for Information and Neural Networks (CiNet), National Institute of Information and Communications Technology
3. Center for Magnetic Resonance Research, University of Minnesota

Short title: Broadband spectral responses in visual cortex

Contact information:
Eline Kupers
Department of Psychology, New York University
New York University
6 Washington Place, Room 959
New York, NY 10003
eline.kupers@nyu.edu

Acknowledgments: This study was supported NEI grant R00-EY022116 (J.W.), and NIMH grant R01-MH111417 (J.W.).

Abstract

Currently, non-invasive methods for studying the human brain do not reliably measure spike-rate-dependent signals, independent of other responses such as hemodynamic coupling (fMRI) and subthreshold neuronal synchrony (oscillations and event-related potentials). In contrast, invasive methods – animal microelectrode recordings and human electrocorticography (ECoG) – have recently measured broadband power elevation in field potentials (~50-200 Hz) as a proxy for the locally averaged spike rates. Here, we sought to detect and quantify stimulus-related broadband responses using magnetoencephalography (MEG) in individual subjects. Because extracranial measurements like MEG have multiple global noise sources and a relatively low signal-to-noise ratio, we developed an automated denoising technique, adapted from (Kay et al., 2013), that helps reveal the broadband signal of interest. Subjects viewed 12-Hz contrast-reversing patterns in the left, right, or bilateral visual field. Sensor time series were separated into an evoked component (12-Hz amplitude) and a broadband component (60–150 Hz, excluding stimulus harmonics). In all subjects, denoised broadband responses were reliably measured in sensors over occipital cortex. The spatial pattern of the broadband measure depended on the stimulus, with greater broadband power in sensors contralateral to the stimulus. Because we obtain reliable broadband estimates with relatively short experiments (~20 minutes), with a sufficient signal-to-noise-ratio to distinguish responses to different stimuli, we conclude that MEG broadband signals, denoised with our method, offer a practical, non-invasive means for characterizing spike-rate-dependent neural activity for a wide range of scientific questions about human brain function.

Significance Statement

Neuronal activity causes perturbations in nearby electrical fields. These perturbations can be measured non-invasively in the living human brain using EEG and MEG. These techniques have emphasized two kinds of measurements: oscillations and event-related responses. A third type of signal, a stimulus-related increase in power spanning a wide range of frequencies ('broadband'), is routinely measured in invasive recordings, but not with MEG and EEG. This broadband response is of great interest because unlike oscillations and event-related responses, it is correlated with neuronal spike rates. Here we report quantitative, spatially specific measurements of broadband fields in individual human subjects using MEG. These results demonstrate that a spike-rate-dependent measure of brain activity can be obtained non-invasively from the living human brain.

Key words: MEG, spectral analysis, denoising, broadband, visual cortex, steady state visual evoked fields

Introduction

The time-varying electric and magnetic fields near neural tissue provide an indirect but rich source of information about the activity of neural populations (reviewed by Buzsaki et al., 2012). These signals include rapid, 'evoked' responses that are time-locked to stimulus events (Norcia et al., 2015), oscillatory responses (Berger, 1929), and non-oscillatory, broadband signals (Miller et al., 2007; Miller et al., 2009c). Broadband signals associated with sensory or motor tasks have been widely observed in human electrocorticography, or 'ECoG', (Miller et al., 2014) and animal microelectrode recordings (Henrie and Shapley, 2005). The broadband signal is an elevation in spectral power, typically spanning 50 to >200 Hz (Miller et al., 2009b), and has attracted a great deal of attention for several reasons.

First, the broadband signal is correlated with the level of neural activity (multi-unit spiking), and hence provides a way to study population-level spiking activity in a cortical region (Liu and Newsome, 2006; Manning et al., 2009; Ray and Maunsell, 2011). Second, the broadband signal has a smaller point spread function on the cortical surface than low frequency oscillations (8-25 Hz) (Miller et al., 2009c; Hermes et al., 2012b), and is therefore useful both for characterizing local properties of cortex and as a tool for neural prosthetics (Schalk and Leuthardt, 2011). Third, the broadband signal is correlated with a portion of the fMRI response and, together with other field potential measures, can be used to understand neural factors underlying an observed BOLD response (Hermes et al., 2012b; Lima et al., 2014). Finally, because it can be measured at high temporal resolution, the broadband signal is useful for characterizing the temporal dynamics of neuronal activity (Honey et al., 2012; Podvalny et al., 2017).

In contrast to intracranial recordings, in the extracranial measures of electroencephalography (EEG) and magnetoencephalography (MEG), broadband responses have not been widely and reliably observed. One significant challenge in identifying broadband in extracranial measures is that non-neural noise sources, particularly from miniature saccades, can be confounded with experimental designs, making neurally induced broadband responses hard to isolate (Yuval-Greenberg et al., 2008; Yuval-Greenberg and Deouell, 2009, 2011; Carl et al., 2012).

A second challenge in measuring broadband extracranially is that the response is most evident in high frequencies (> 60 Hz), and the signal amplitude at these frequencies is low. While intracranial recordings have relatively high signal-to-noise ratios (SNR) even at these higher frequencies (Miller et al., 2014), EEG and MEG do not (Hämäläinen et al., 1993). Broadband signals can extend to lower frequencies (Harvey et al., 2013; Winawer et al., 2013), but oscillatory processes in lower frequency bands often mask broadband measures in this range (Miller et al., 2009c).

A third challenge is the potential confound between broadband signals and narrowband gamma oscillations. Narrowband gamma oscillations have been successfully measured with MEG and EEG, particularly in visual cortex for high contrast gratings (Hoogenboom et al., 2006; Fries et al., 2008; Muthukumaraswamy and Singh, 2013). The frequency range of these oscillations (30-100 Hz) overlaps the broadband range, but the narrowband and broadband signals reflect biologically different processes (Henrie and Shapley, 2005; Miller et al., 2009b; Ray and Maunsell, 2011; Miller et al., 2014). The ability to measure one does not imply the ability to measure the other.

Here, we sought to measure broadband signals quantitatively in the human brain using a non-invasive method (MEG). In order for this important, spike-dependent signal to be useful, it is necessary to measure it reliably in individual subjects, with a high SNR. A high SNR is essential if this signal will be widely used to study differences across stimuli, tasks, or groups. We developed a novel, automated MEG denoising algorithm adapted from prior fMRI work (Kay et al., 2013). Our experiments were designed to elicit spatially localized neural responses in visual cortex, and eye movements were measured in a subset of subjects to test for possible confounds from non-neural sources.

Methods

Data acquisition

Subjects

Eight subjects (five females), ages 20-42 years (M = 28.4 / SD = 6.7 years) with normal or corrected-to-normal vision participated in the NYU study. An additional 4 subjects (M = 27.0 / SD = 7.4 years) participated in the same experiment at Center for Information and Neural Networks (CiNet), National Institute of Information and Communications Technology (NICT) in Osaka, Japan. Observers provided written informed consent. The experimental protocol was in compliance with the safety guidelines for MEG research and was approved by the University Committee on Activities involving Human Subjects at New York University and by the ethics committee of the National Institute of Information and Communications Technology (NICT).

Display

Stimuli were generated using MATLAB (MathWorks, MA) and PsychToolbox (Brainard, 1997; Pelli, 1997) on a Macintosh computer. NYU: Images were presented using an InFocus LP850 projector (Texas Instruments, Warren, NJ) with a resolution of 1024 x 768 pixels and refresh rate of 60 Hz. Images were projected via a mirror onto a front-projection translucent screen at a distance of approximately 42 cm from the subject's eyes (field of view: 22 deg × 22 deg). The display was calibrated with the use of a LS-100 luminance meter (Konica Minolta, Singapore) and gamma-corrected using a linearized lookup table. CiNet: The display parameters were similar, except that the projector was PT-DZ680 (Panasonic, Japan), with 800 x 600 resolution and 60 Hz, and 61 cm viewing distance.

Stimuli

The stimuli were contrast-reversing dartboard patterns (12 square wave contrast reversals per second), windowed within either a half circle (left or right visual field) or full circle (bilateral visual field) aperture, with a diameter of 22 degrees at NYU (26 degrees at CiNet). Mean luminance gray (206 cd/m^2 (NYU), 83 cd/m^2 (CiNet)) was used as background color for the dartboards and was shown in the full field during blank trials between stimulus periods (Figure 1).

Experimental design

One *run* consisted of six seconds flickering 'on' periods, alternated with six seconds 'off' mean luminance periods, repeated 6 times (72 seconds). The order of the left-, right- or both-visual field apertures was random. There was a fixation dot in the middle of the screen throughout the run, switching between red and green at random intervals (averaging 3 seconds). The subjects were instructed to maintain fixation throughout the run and press a button every time the fixation dot changed color. The subjects were asked to minimize their blinking and head movements. After every 72-second run, there was a short break (typically 30-s to 1 minute). Each subject participated in 15 runs.

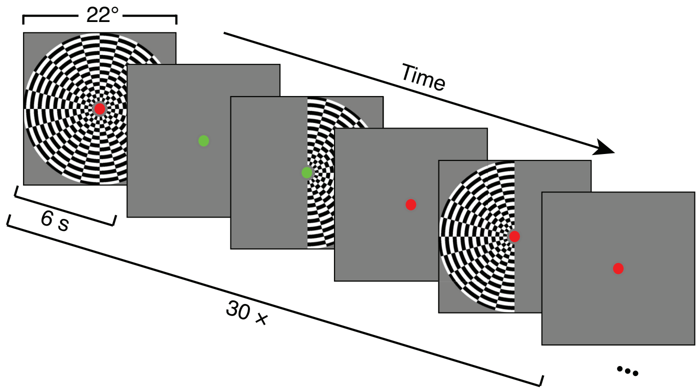

Figure 1. Overview of experimental design. Large-field on-off stimuli were presented in 6-s blocks consisting of either both-, left-, or right-hemifield flicker, alternating with 6-s blocks of blanks (mean luminance). A run consisted of six stimulus and six baseline blocks, after which the observer had a short break. The figure shows the first half of one run. Within a run, the order of both-, left-, and right-field flickering periods was randomized. Fifteen runs were obtained per observer, so that there were 30 repetitions of each stimulus type across the 15 runs. The fixation dot is increased in size for visibility. Actual fixation dot was 0.17 degrees in radius (6 pixels).

MEG signal acquisition

Data for the main experiment were acquired continuously with a whole head Yokogawa MEG system (Kanazawa Institute of Technology, Japan) containing 157 axial gradiometer sensors to measure brain activity and 3 orthogonally-oriented reference magnetometers located in the dewar but away from the brain area, used to measure environmental noise. The magnetic fields were sampled at 1000 Hz and were filtered during acquisition between 1 Hz (high pass) and 200 Hz (low pass).

In a subset of subjects (S6-S8), eye movements were recorded by an EyeLink 1000 (SR Research Ltd., Osgoode, ON, Canada). Right eye position data were continuously recorded at a rate of 1000 Hz. Calibration and validation of the eye position was conducted by having the subject saccade to locations on a 5-point grid. Triggers sent from the presentation computer were recorded by the EyeLink acquisition computer. The same triggers were recorded simultaneously by the MEG data acquisition computer, allowing for synchronization between the eye-tracking recording and MEG recording.

The 4 data sets acquired with an Elekta Neuromag at CiNet and were pre-processed in MATLAB (MathWorks, MA, USA) using the identical code and procedure. The CiNet data were acquired as 102 pairs of planar gradiometer signals (204 sensors). Data were analyzed from each of the 204 gradiometers separately and paired into 102 locations for mesh visualization (e.g., the broadband signal-to-noise-ratio for sensor 121 and 122 out of 204 would be averaged to show one signal-to-noise-ratio in the position of sensor 61 out of 102).

Data analysis

Reproducible computation and code sharing

All analyses were conducted in MATLAB. In the interest of reproducible computational methods, both the analysis code and the MEG data for all results reported in this paper will be publicly available via the Open Science Framework at the url https://osf.io/c59sh/ (doi 10.17605/OSF.IO/C59SH). Figures 2-15 (except 3) can be reproduced by running scripts from the GitHub repository of the form *dfdMakeFigure4.m*, or the master script *dfdMakeAllFigures.m*.

MEG preprocessing

For some analyses, data were environmentally denoised using published algorithms prior to any further analysis. This enabled us to compare data denoised with our new algorithm alone, or with our new algorithm following environmental denoising. For the NYU data, we used either of two algorithms. One was the continuously adjusted least-square method (CALM; Adachi et al., 2001), applied to data with a block length of 20 seconds (20,000 time samples). The second algorithm was time-shifted principal component analysis (TSPCA; de Cheveigne and Simon, 2007), with a block length of 20 seconds and shifts of up to +/- 100 ms in 1 ms steps. For the CiNet data, the environmental denoising algorithm was temporal signal space separation ('tSSS') (with default parameters, e.g. inside and outside expansion orders of 8 and 3, respectively; 80 inside and 15 outside harmonic terms; correlation limit of 0.98).

The FieldTrip toolbox (Oostenveld et al., 2011) was used to read the data files (either environmentally-denoised or raw). For all subsequent analyses, custom code was written in MATLAB. Using either the environmentally-denoised data or raw data, the signals were divided into short epochs. Each stimulus type (left-, right-, or both-hemifield, or blank) was presented in 6-s blocks, and these blocks were divided into 6 non-overlapping 1-s epochs. We discarded the first epoch of each 6-s block to avoid the transient response associated with the change in stimulus. After epoching the data, we used a simple algorithm to detect outliers. We first defined a 'data block' as the 1-s time series from one epoch for one sensor. So a typical experiment consisted of ~170,000 data blocks (157 sensors x 1080 1-s epochs). We computed the standard deviation of the time series within each data block, and labeled a block as 'bad' if its standard deviation was more than 20 times smaller or 20 times larger than the median standard deviation across all data blocks. The time series for bad data blocks were replaced by the time series spatially interpolated across nearby sensor (weighting sensors inversely with the distance). Further, if more than 20% of data blocks were labeled bad for any sensor, then we removed the entire sensor from analysis, and if more than 20% of data blocks were bad for any epoch, then we removed the entire epoch from analysis. Typically, two to seven sensors and 2%-4% of the epochs were removed per session for the NYU data. For the CiNet datasets, almost no sensors or epochs were removed (one sensor and one epoch across all data sets). These preprocessing steps were implemented with *dfdPreprocessData*.m.

Computation of stimulus locked and broadband responses

Data were summarized as two values per sensor and per epoch: a stimulus-locked and a broadband power value. These calculations were done by first computing the Fourier transform of the time series within each epoch (Figure 2A,B).

The stimulus-locked signal was then defined as the amplitude at the stimulus locked frequency (12 Hz). The broadband response was computed as the geometric mean of the power across frequencies within the range of 60-150 Hz, excluding multiples of the stimulus locked frequency (see also Figure 2 AB). The geometric mean is the exponential of the average of the log of the signal. We averaged in the log domain because log power is better approximated by a normal distribution than is power, which is highly skewed. These two calculations converted the MEG measurements into a broadband and a stimulus-locked summary metric, each sampled once per second (Figure 2C). The two summary metrics were computed by the functions *getstimlocked.m* and *getbroadband.m*.

We then bootstrapped across epochs to compute confidence intervals on the signal estimates (per sensor and per condition). For each of 1000 bootstraps, we sampled *n* epochs with replacement, where *n* is the total number of epochs in the experiment. We then computed the average response across epochs for each stimulus condition, minus the average across blank epochs. This provided one summary measure for each of the three stimulus conditions and each of the two dependent measures (broadband and stimulus locked) for each of the 1000 bootstraps. Finally, we took the median across bootstraps as the estimate of signal and half of the 68% confidence interval across bootstraps as the estimate of the noise (Figure 2D,E). For some analyses, the ratio of these values was defined as the signal-to-noise ratio (SNR).

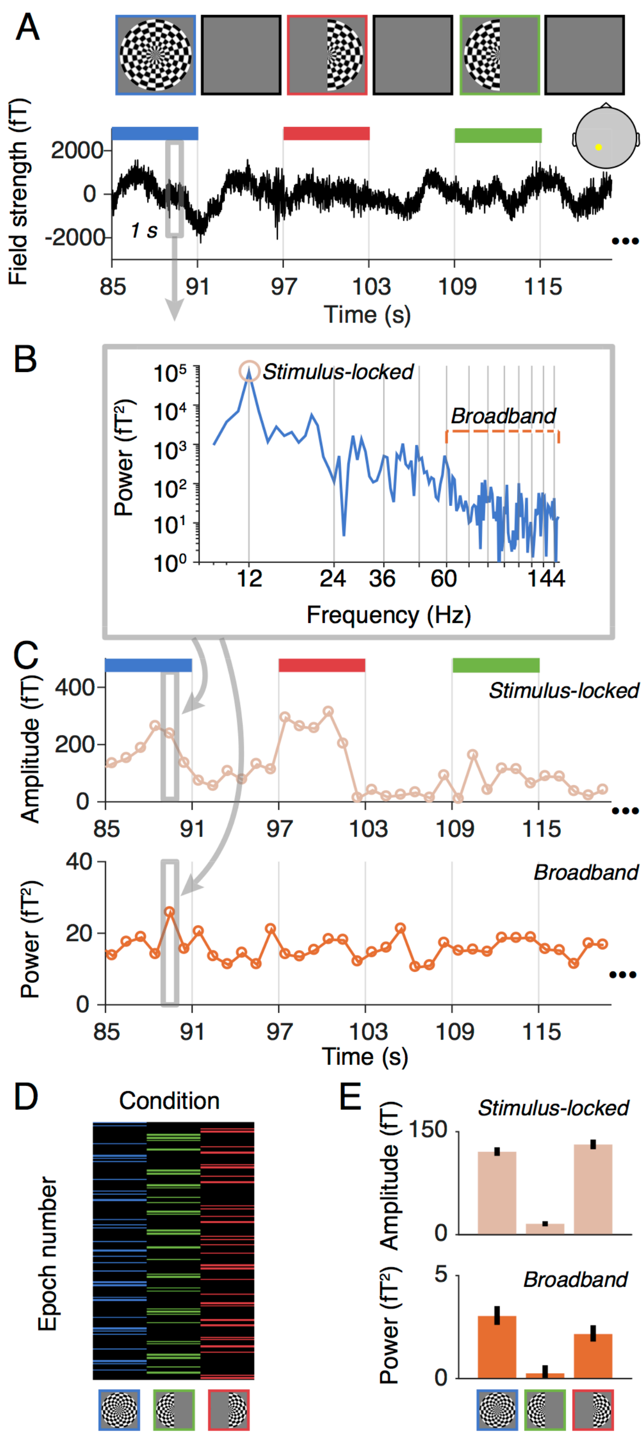

Figure 2. Data analysis without denoising. A. The time series for each sensor were epoched into non-overlapping one-second periods. BC. The time series in each epoch was fast Fourier transformed and then summarized as two values, a stimulus-locked value (amplitude of the fast Fourier component at the stimulus frequency), and a broadband value (mean of the log power of all frequencies from 60-150 Hz, excluding those within +/- 1 Hz of stimulus harmonics). D. The summary of conditions is shown as a matrix, where each column corresponds to one of the three stimulus conditions, and the number of rows is equal to the total number of epochs across the session. Rows with no color are blank epochs. E. Summary metrics were computed separately for the stimulus-locked values and broadband measures, yielding three measures per sensor per data type. The summary metric was the mean across condition minus the mean across blanks, bootstrapped 1000 times. The bar plot show the median and the 68% confidence interval based on 1000 bootstraps.

MEG Denoise Algorithm

Extracranial measurements like MEG have multiple global noise sources and a relatively low signal-to-noise ratio compared to intracranial measures, especially for high frequency signals. In order to increase the signal-to-noise ratio, we developed a denoising technique that helps reveal the broadband signal of interest. A denoising algorithm developed for fMRI ('GLMdenoise'; (Kay et al., 2013)) was adapted for MEG to project out noise from the data for each epoch in each sensor. The logic behind the algorithm is that many sources of noise are global, and therefore spread across sensors. The algorithm identifies sensors that have no stimulus-related response (the 'noise pool'), and uses these sensors to define noise components. The noise components are then projected out from all sensor time series in each epoch.

Noise pool selection

The noise pool was defined as the 75 (NYU) or 100 (CiNet) sensors with the lowest stimulus-locked SNR across conditions. The SNR was computed by (a) dividing the median response across bootstraps by the variability across bootstraps (half of the 68% confidence interval) for each condition, and (b) taking the maximum of the three values (corresponding to the three stimulus conditions) for each sensor.

We used the stimulus-locked signal to identify the noise pool because this signal had a very high SNR, and could easily by measured prior to running our denoise algorithm, and because we assumed (and confirmed by inspection) that sensors with broadband responses also had stimulus-locked responses.

For most observers, most of the sensors in the noise pool were located over the front of the head (see for example Figure 3A).

Filtering of time series

As described above, the broadband summary metric was derived from power at a limited range of temporal frequencies (60-150 Hz, excluding multiples of the stimulus frequency). After defining the noise pool, the time series of all sensors in all epochs were filtered to remove signal at all frequencies not used to compute the broadband signal. Hence the remaining time series contained power only at frequencies defining the signal of interest. This step was important because the noise pool, though selected for a low stimulus-locked SNR, could nonetheless have contained a small, residual stimulus-locked signal. This residual signal would have been correlated with the experimental design (larger when stimuli were present than absent) and hence projecting it out of the data could have caused a systematic bias (see the script *denoisingProjectingInVariance.m*).

PCA

Following filtering, the next step in the algorithm was principal component analysis (PCA). This identified the common components of the time series across the sensors in the noise pool. PCA was computed separately for each 1-s epoch (Figure 3C). This means that denoising occurred at the same temporal scale (1 second) as the computation of the summary metrics. This differs from some denoising algorithms, in which noise regressors are identified over a much longer time period, e.g., several minutes (Vigario, 1997). Denoising at a short-time scale can be advantageous if the spatial pattern of the noise responses is not consistent across the entire experiment. As a control comparison, we also ran our algorithm by identifying PC time series on the entire duration of the experiment (~20 minutes) rather than epoch by epoch. (See Results, 'Control analyses for MEG Denoise algorithm'.)

Projecting out PCA components

The first one to ten principal components (PCs) in each epoch were projected out of the time series for all sensors, using linear regression. This resulted in ten new data sets: One with PC 1 projected out, one with PC 1 and 2 projected out, etc. up to 10 PCs projected out (Figure 3D). After projecting out the noise components, we summarized the data into a stimulus-locked and broadband component as described in Figure 2.

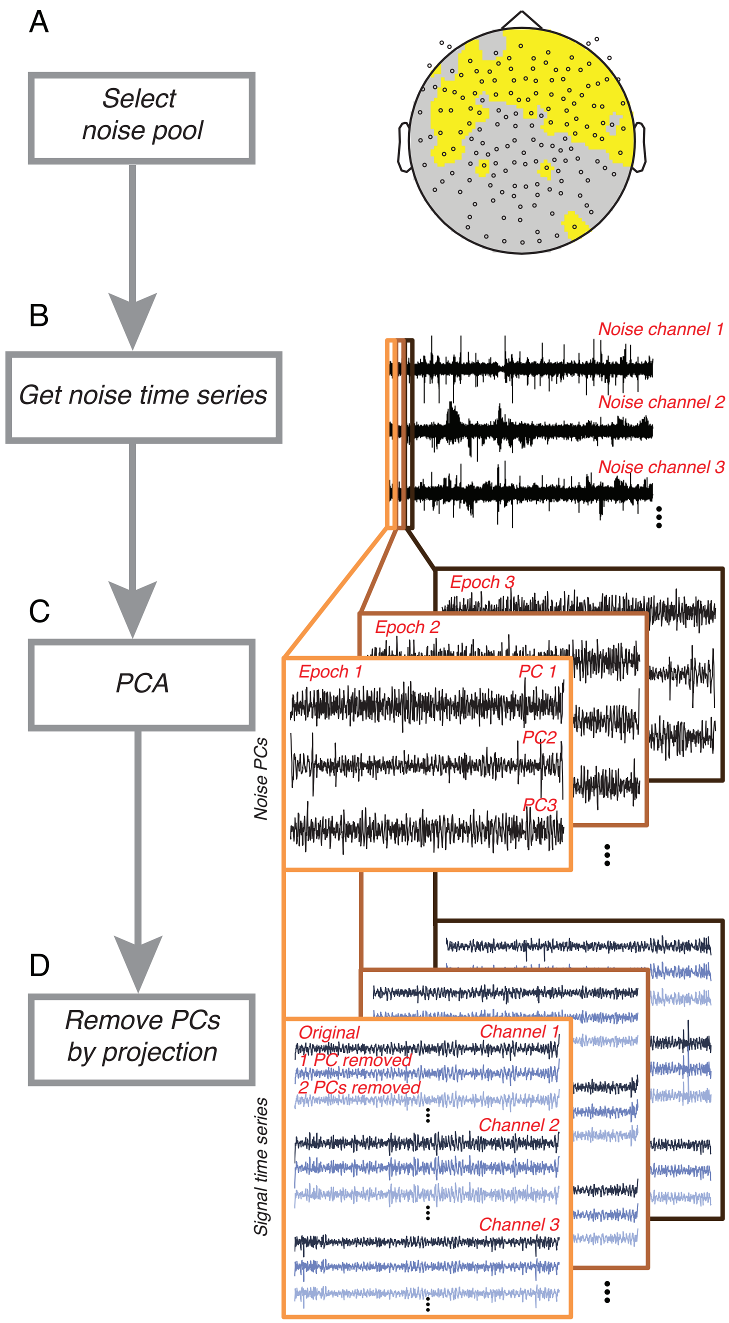

Figure 3. Denoising procedure. Following an estimate of response reliability computed from non-denoised data (Figure 2), the algorithm first selects a noise pool. **A.** The noise pool is comprised of sensors whose SNR from the evoked (stimulus-locked) component falls below a threshold. **B.** The time series from each sensor in the noise pool is then filtered to remove components that do not contribute to the broadband computation. **C.** Principal component analysis is then computed within each epoch. **D.** for each epoch, the first *n* PCs are projected out from the time series of all sensors, yielding *n* new data sets. For each new data set, broadband responses were recomputed, as in Figure 2.

Statistical comparisons

To assess the effect of the MEG Denoise algorithm on the broadband SNR, we compared the broadband SNR after applying MEG Denoise to the broadband SNR either without denoising or after applying other denoising algorithms. To make these comparisons, we first identified 10 sensors of interest from each subject. These sensors of interest were the 10 with the highest SNR in any of the three stimulus conditions, either before or after denoising, excluding sensors from the noise pool. For each of the three stimulus conditions, we then took the average SNR from these 10 sensors without denoising or after applying MEG Denoise or another denoising algorithm. Finally, we conducted two-tailed t-tests, paired by subject (n=8), between the broadband SNR after MEG Denoise to the broadband SNR without denoising (or with another algorithm). The t-tests were conducted separately for each of the three stimulus conditions (both-hemifield, left-hemifield, and right-hemifield).

Control analyses

To investigate the validity of our algorithm, we ran multiple control analyses. In particular, it is important to rule out the possibility that the denoising algorithm produces significant results even when the data contains no sensible signal. To test this, we compared the difference in SNR of denoised data with the following controls: (1) phase-scrambling the PC time series, and (2) using all sensors to define the noise with PCA rather than only a subset of sensors that have little to no stimulus-locked signal. We also assessed the effect of identifying and projecting out PC time series equal in length to the entire experiment (~20 minutes), rather than PC time series matched in length to our analysis epochs (1-s). This comparison tested the assumption that denoising in shorter epochs was advantageous, possibly due to the pattern of noise sources differing over the course of the experiment.

Eye tracking analysis

Since an increase in microsaccade rate can induce broadband spectral components in extracranial measurements such as EEG or MEG (Yuval-Greenberg et al., 2008; Keren et al., 2010), we checked in three NYU subjects (S6-S8) whether there was a difference in rate between the 'off' baseline periods and 'on' stimulus periods, and within the three stimulus (both-, right-, left-hemifield) conditions. Microsaccades were identified as changes in position with above a relative velocity threshold (6°/s) and a minimum duration of 6 ms, as reported in Engbert & Mergenthaler (2006) to analyze rate and direction of microsaccades as well as separating MEG data into epochs that did and did not contain microsaccades.

Results

A large field 'on-off' stimulation experiment was used to characterize the stimulus-locked (steady state evoked field, 'SSVEF') and broadband responses in visual cortex measured with MEG. The two measures are reported below, both prior to and after applying our new denoising algorithm.

Stimulus-locked and broadband signals measured with MEG

In each stimulus condition (left-, right-, and both-hemifield), the stimulus contrast reversed 12 times per second, so the stimulus-locked signal was measured at 12 Hz and harmonics. Because the largest component was at 12 Hz, we defined the stimulus-locked signal for a particular stimulus condition as the amplitude at 12 Hz, averaged over all 1-second epochs with that stimulus (typically ~180 epochs) computed for each of the 157 sensors in each subject (Figure 4; see Methods for details). The broadband signal was computed by averaging the log power across frequencies between 60 and 150 Hz, excluding multiples of the stimulus frequency (12 Hz), and then exponentiating the mean (Figure 4 inset; see Methods for details).

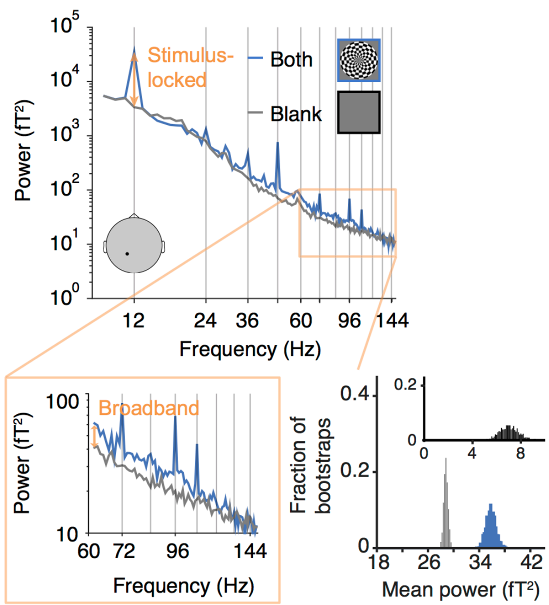

Figure 4. Example response to flickering large-field stimulus. The main panel plots the spectral power, averaged across 180 1-s epochs, during which the subject viewed either the both-hemifield stimulus (blue line) or a blank screen at mean luminance (gray line). The black dot on the schematic head indicates the location of the sensor. The peak at 12 Hz corresponds to the frequency of dartboard contrast reversals, and is a measure of the stimulus-locked component (orange arrow). The lower inset zooms in on higher frequencies to emphasize the broadband component, most evident in this example data set as a spectral power elevation spanning 60 to 150 Hz. The increase in the broadband response of the stimulus condition relative to the blank condition is shown by the orange arrow. The histograms on the right show the broadband level separately for the stimulus condition (blue) and the blank condition (gray), and the difference between them (black), computed 1000 times by bootstrapping over epochs in the experiment. Data from subject S1. Made with function *dfdMakeFigure4.m*.

Both the stimulus-locked and broadband signals were largest in medial, posterior sensors, as expected from activations in visual cortex (Seki et al., 1996). For the stimulus-locked signal, the both-hemifield condition tended to produce broadband signals in bilateral posterior sensors, whereas the single-hemifield conditions produced responses that were lateralized, with higher SNR contralateral to the stimulus. This pattern could be seen in an example subject and in the average across subjects (Figure 5). The lateralization of the stimulus-locked signal was less clear in the average across subjects due to imperfect alignment of the sensors showing the largest differential response to the left- and right- hemifield stimuli. In each of the 8 individual subjects and in each of the 3 conditions, the stimulus-locked response was evident, with the signal at least 10x above the noise (data not shown).

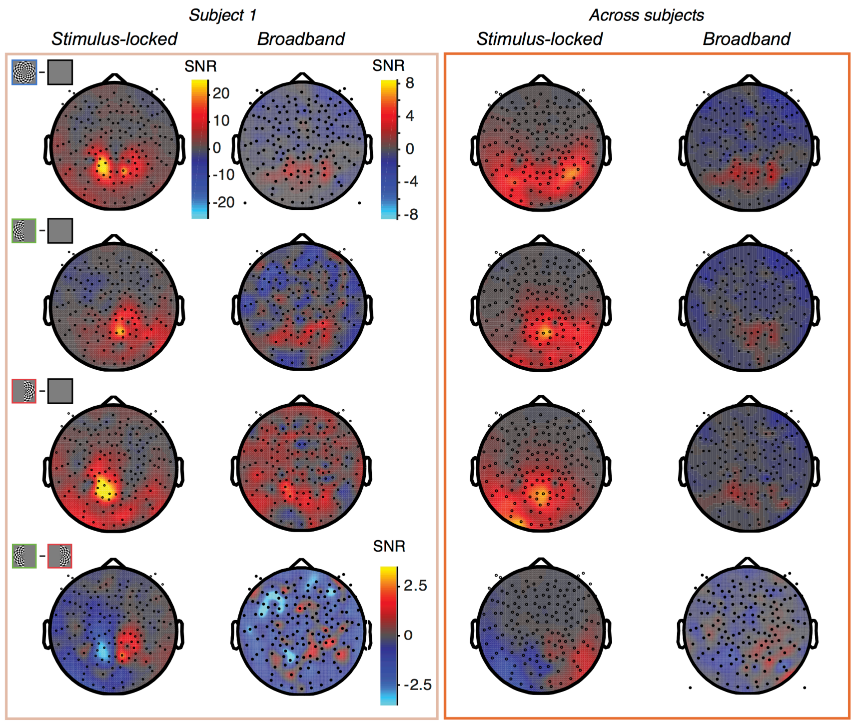

Figure 5. Topographic map of stimulus-locked and broadband responses. Data from subject S1 (left) and averaged across subjects S1-S8 by sensor (right). The top 3 rows show data from the 3 stimulus conditions (both-, left-, and right-hemifield) compared to blank, and the lower row shows data as the left-only minus right-only conditions. The dependent variable plotted for the single subject data is the signal-to-noise ratio at each sensor, computed as the mean of the contrast (stimulus minus blank) across bootstraps divided by the standard deviation across bootstraps (bootstrapped over epochs). For the group data, the signal-to-noise ratio is the mean of the subject-specific SNRs at each given sensor. The same scale bar is used for all stimulus-locked plots. For the broadband plots, one scale bar is used for the first three rows, and a different scale bar with a smaller range is used for the fourth row. Made with *dfdMakeFigure5.m*.

The spatial pattern of broadband signals was qualitatively similar to the spatial pattern of the stimulus locked signal, with bilateral posterior responses in the both-hemifield condition, and lateralized responses in the single-hemifield conditions (Figure 5, individual example and group-averaged data). However, the broadband responses had much lower signal-to-noise than the stimulus-locked responses, and in many of the individual subjects, broadband was not evident in one or more conditions (data not shown). The broadband responses were less reliable for the left- and right-hemifield conditions than for the both-hemifield conditions.

The fact that broadband responses were evident in a few subjects in some conditions indicates that it is possible to measure broadband fields with MEG. However, if this signal cannot be measured reliably in many subjects and many conditions, then the practical value of measuring broadband with MEG is limited. This motivated us to ask whether denoising the MEG data could unmask broadband signals, making it more reliable across subjects and stimulus conditions.

Denoising increases the broadband SNR by reducing variability

The MEG data were denoised using a new algorithm as described in detail in the Methods section. In brief, for each subject a subset of sensors that contained little to no stimulus-locked responses were defined as the noise pool. Once the noise-pool was defined, the time series in each sensor and in each epoch was filtered to remove all signals not contributing to the broadband measurement. Global noise regressors were then derived by principal component analysis from the filtered time series in the noise pool in each 1-s epoch. The first 10 PCs were projected out of the data in each sensor, epoch by epoch. The remainder of the analysis was identical to that used in the non-denoised data set (Figure 2).

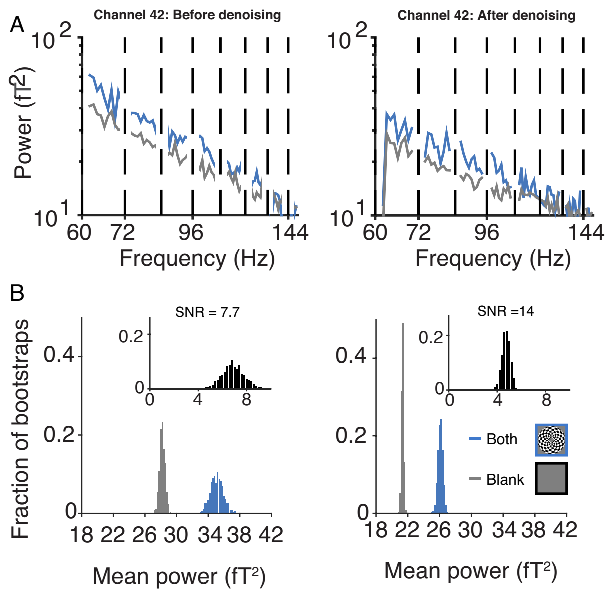

Figure 6. Effect of denoising on broadband response. (A) The upper panel shows the power spectra from sensor 42, subject 1, averaged across 178 epochs with the both-hemifield stimulus (blue) and blank screen (gray). The left panel is prior to denoising and is identical to the inset in figure 4, except that harmonics of stimulus-locked frequencies have been removed. The right panel is the same as the left, except after denoising. (B) The lower panel shows the distributions of the bootstrapped broadband power for the both-hemifield (blue), blank (gray), and both-hemifield minus blank (black, inset), prior to denoising (left) and after denoising (right). The SNR is defined as the median of the difference distribution divided by half of the 68% confidence interval in the difference distribution (7.7 prior to denoising, 14.0 after). The effects of denoising are to reduce the mean power, and more importantly, reduce the standard deviation across epochs. Made with *dfdMakeFigure6.m*.

We first illustrate the effect of denoising with an example from a single sensor in one subject (Figure 6). This sensor showed a broadband response both prior to, and after, denoising. The benefit of denoising was not evident when comparing the mean power spectra before and after denoising (Figure 6A). Denoising did not reduce the variability in power across frequencies, nor did it increase the separation in the spectra for the contrast stimulus and the blank. Instead, the effects of denoising are better appreciated by examining the variability across epochs rather than across frequencies (Figure 6B). The biggest effect is that the broadband power estimates became less variable across epochs, both for the blank condition and the stimulus condition. This is indicated by the narrower distributions in the response amplitudes for the two conditions (Figure 6B, main panels) and for the difference between conditions (Figure 6B, insets). The standard deviation of the difference distributions decreased more than two-fold (from 0.79 to 0.35) as a result of denoising.

There are two other secondary patterns evident in these distributions. First, the mean broadband power of both the blank and stimulus condition decreased as a result of denoising (for the both-hemifield condition, 35.8 versus 26.1, prior to versus after denoising; for the blank, 28.7 versus 21.4). This was expected because projecting out signal reduces power. Second, the contrast between the two conditions (difference between the means) reduced: 7.0 prior to denoising versus 4.8 after denoising. The combination of these two effects was that the *percent difference* was little changed, with broadband power from the contrast-stimulus about 25% more than for the blank before and after denoising. Hence denoising did not increase the estimate of the percent signal change.

It is important to consider how these effects interact. Because the reduction in variability across epochs was the biggest effect of denoising (more than 2-fold), there was more than a doubling of SNR, computed as the median divided by the variability of the difference distribution[1]. In sum, the spectral plots show that the variability in power *across frequencies* was little affected by denoising (Figure 6A), whereas the distribution plots show that the variability in total broadband power *across epochs* was reduced considerably (Figure 6B).

We now consider the effect of denoising across sensors, subjects, and stimulus conditions. Projecting out noise PCs substantially increased the signal-to-noise ratio of the broadband measurement in visually responsive sensors. For example, in the both-hemifield condition for subject S1, the median SNR of the 10 most visually responsive sensors increased from 5 to 10 after denoising (Figure 7A, blue solid line), similar to the example sensor shown earlier (Figure 6B). In contrast, the SNR of the 75 sensors in the noise pool was relatively unaffected by denoising (Figure 7A, blue dashed line). This was expected because sensors in the noise pool were unlikely to distinguish stimulus from blank. Across the 8 subjects in the both-hemifield condition, taking the mean of the 10 most visually responsive sensors for each subject, the SNR increased about 3-fold (from 1.6 to 5.0), with a numerical increase in every subject (Figure 7B). Because the SNR stabilized in all subjects with 10 or fewer PCs projected out, in subsequent analyses, for simplicity we report the effects of denoising with exactly 10 PCs. A comparison of the SNR before denoising (0 PCs projected out) and after (10 PCs projected out) summarized across all subjects and the three stimulus conditions shows increases in SNR for every subject in all conditions (Figure 7C) (p=0.0001, p=0.0007, p=0.0022 for two-tailed t-tests, 0 v 10 PCs, for both-, left-, and right-hemifield conditions, respectively).

[1] There are many ways to define 'signal', 'noise', and therefore the signal-to-noise-ratio ('SNR'). Here we define **signal** as the difference in broadband power between a condition of interest and blank, and we define **noise** as the variability in the signal estimate when we bootstrap over epochs (half of the 68% confidence interval). According to these definitions, denoising caused the signal in the example sensor to go down, and the noise to go down even more, and hence the **SNR** went up. Alternatively, one could define signal as the percent increase over baseline. By this definition, signal was about 25% before *and* after denoising in the example sensor. One could also define the signal as the broadband power of a single condition without subtracting the baseline. By this definition, denoising caused the full-field stimulus signal to go down, and the blank stimulus signal to go down. By this alternate definition, denoising almost always causes a signal decrease, because denoising projects out regressors, which tends to remove power.

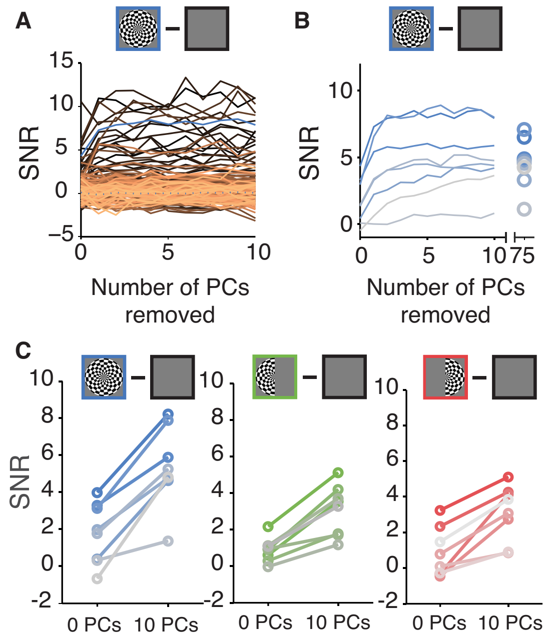

Figure 7. Effect of denoising on broadband SNR. (A) SNR as a function of the number of PCs projected out in subject S1 for the both-hemifield stimulus. Each line is one sensor. The heavy blue line is the mean of the 10 sensors with the highest SNR, as measured either before or after denoising. (B) SNR as a function of PCs projected out in each of 8 subjects for the both-hemifield stimulus. Each line is the mean across the 10 sensors with the highest SNR in one subject. The rightmost points indicate the effect of projecting out all 75 PCs. (C) SNR before denoising (0 PCs projected out) and after denoising (10 PCs projected out) for each stimulus condition. Each line is the mean of the 10 sensors with the highest SNR for one subject in one stimulus condition. Color saturation corresponds to the subject number (highest to lowest saturation, subjects 1-8, respectively). Made with *dfdMakeFigure7.m*.

In principle, the SNR increases could have arisen from increased signal, decreased noise, or both. To distinguish among these possibilities, we compared the signal level alone and the noise level alone before and after denoising. As in prior results, the signal was defined as the difference in broadband power between the contrast pattern and the blank (median across bootstraps), and the noise was defined as the variability of this difference metric (half of the 68% confidence interval across bootstraps). For all three stimulus conditions in most subjects, the signal was largely unaffected by denoising, staying at a similar level or decreasing slightly, while the noise level went down substantially (Figure 8). These analyses indicate that the increase in SNR from denoising (Figure 7) was caused by a reduction in epoch-to-epoch variability of the broadband signal level, and not by an increase in the signal level, consistent with the results of the single example sensor (Figure 6). Expressed as a percentage increase over baseline, the broadband response to the both-hemifield stimulus after denoising was ~10.9±1.7% averaged across the top 10 sensors in each subject (mean ± sem across subject), and 12.6%±1.6% for the top 5 sensors. This contrasts with the much larger stimulus-locked response, which was a nearly 8-fold increase over baseline even prior to denoising (678%±226% increase over baseline for the top 5 sensors).

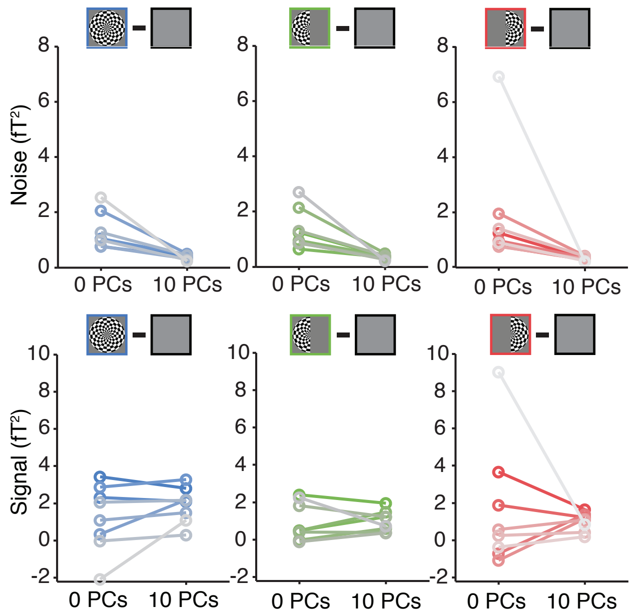

Figure 8. Effect of denoising on the broadband signal and noise. Noise (upper) and signal (lower) before and after denoising in each of three stimulus conditions. Plotting conventions as in Figure 7c. Made with *dfdMakeFigure8.m*.

The effect of denoising the broadband signal was not uniform across the sensor array. In general, sensors where we expected visual activity (over the posterior, central part of the head) showed increased SNR following denoising. In the example subject S1 as well as the average across subjects, the denoised broadband response was observed in bilateral sensors for the both-hemifield condition, and with a contralateral bias (relative to the midline) in the two lateralized conditions (Figure 9). For the both-hemifield stimulus, broadband responses were evident in sensors over the posterior, middle of the head in most individual subjects (Figure 10).

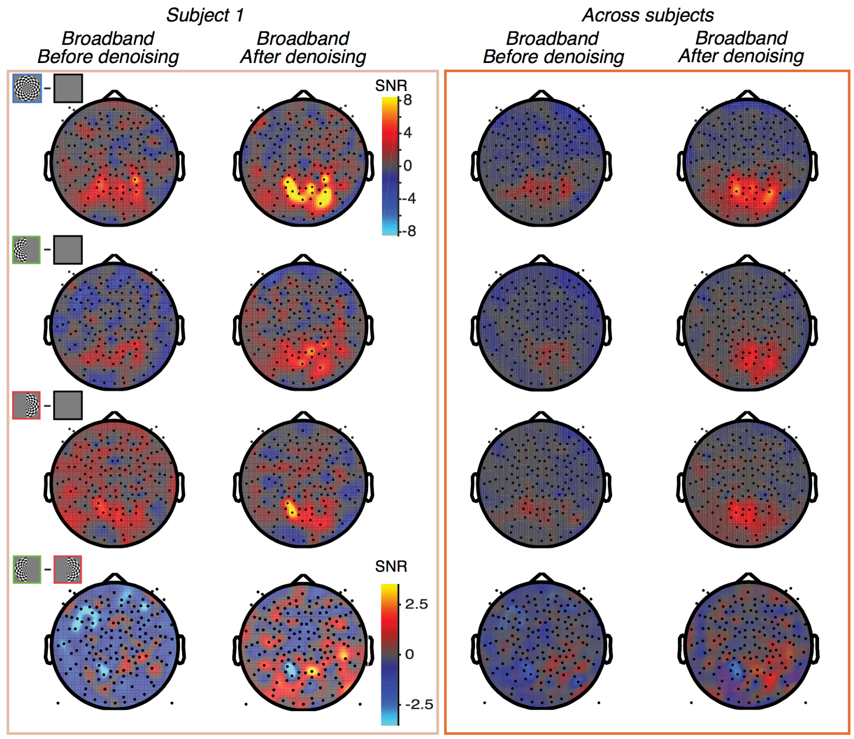

Figure 9 Topographic map of broadband SNR before and after denoising. Data from subject S1 (left) and averaged across subjects S1-S8 by sensor (right). The top 3 rows show data from the 3 stimulus conditions (both-, left-, and right-hemifield) and the fourth row shows the difference between the left-only and right-only conditions. The fourth row uses a different scale bar from the other 3 rows. The columns show data before and after denoising. Made with *dfdMakeFigure9.m*.

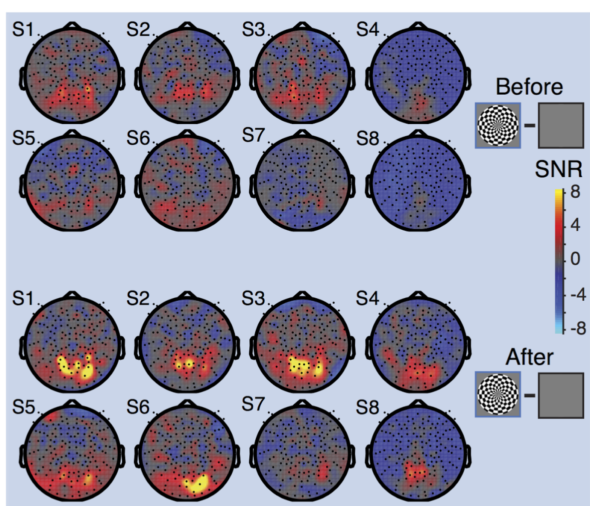

Figure 10 Topographic maps of broadband SNR in individual subjects after denoising. Head plots show the SNR for the both-hemifield stimulus, before denoising (above) and after denoising (below). Made with *dfdMakeFigure10.m*.

Control analyses for MEG Denoise algorithm

To validate the assumptions in our denoising algorithm, we ran three control analyses. In one control analysis, we concatenated all epochs to derive noise regressors from the whole experimental time series (Figure 11, 2nd bar, compared to using the default of 1-s epochs to derive noise regressors – 1st bar). The elevation in broadband SNR was significantly less when we concatenated all epochs (p = 0.0016, p = 0.0023 and p = 0.0447, for the three stimulus conditions respectively). In the second control analysis, the noise pool included all sensors rather than only those sensors that were not visually responsive. Here, the noise regressors included some signal as well as noise, and hence should be of less benefit. This expectation was confirmed, in that there was no increase in SNR when the algorithm was run with the omission of the noise-pool-selection step (Figure 11, 3rd bar, p = 0.0014, p = 0.0015 and p = 0.0020 for the three stimulus conditions respectively). In a 3rd control analysis, we phase-scrambled each of the epoch-by-epoch noise time series. The phase-scrambled regressors were temporally uncorrelated with the actual time series in the noise. As a result, we found no change in SNR levels (Figure 11, fourth bar, p = 0.0001, p = 0.0003 and p = 0.0017).

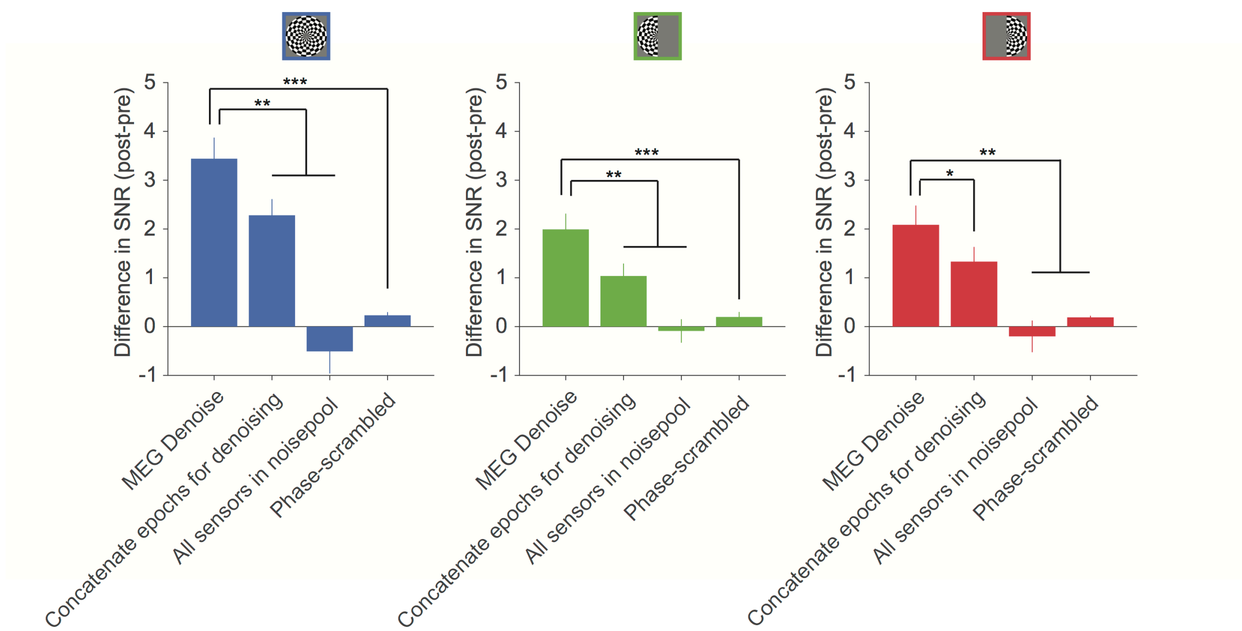

Figure 11. Comparison of MEG Denoise to control analyses. When the denoising algorithm derives noise regressors from the whole experimental time series ('Concatenate epochs for denoising'), the amount of SNR gain is significantly less than the standard MEG Denoise (regressors derived separately from each 1-s epoch). When the noise regressors are derived from all sensors ('All sensors in noisepool'), or when the time series of the regressors are phase-scrambled, there is little or no change in SNR for all three stimulus conditions. Statistical significance is computed by a 2-tailed t-test, paired by subject, between denoising analyses. Statistical significance is indicated by * = p < 0.05, ** = p < 0.01, *** = p < 0.001 between the MEG Denoise algorithm and each of the other controls. Made with *dfdMakeFigure11.m*.

Other denoising algorithms

To assess how other existing denoising algorithms affect our measurement of broadband power, and how they interact with our new denoising algorithm, we ran two different denoising algorithms, either alone or in combination with MEG Denoise. The two algorithms we tested were CALM, or continuously adjusted least-square method (Adachi et al., 2001) and TSPCA, or time-shift principal component analysis (de Cheveigne and Simon, 2007). Both of these make use of reference MEG sensors which face away from the head and measure environmental rather than physiological fields. By design, these algorithms project out time series from the subspace spanned by the reference sensors, thereby reducing environmental noise, but not physiological noise. Applying either one of these two algorithms alone to the 8 data sets reported above increased the broadband signal-to-noise ratio, evident in the group-averaged sensor plots (Figure 12A, columns 3-4 versus column 2), and the increased SNR in the 10 most responsive sensors (Figure 12B, 2nd and 3rd bar versus 1st bar in each plot).

In planned comparisons, we evaluated the SNR increase of each algorithm or combination of algorithms to the increase from MEG Denoise alone. The increase from each of the two environmental algorithms alone was significantly less than that from our new MEG Denoise algorithm (Figure 12A, column 5 versus columns 3-4; Figure 12B, 4th bar versus 2nd and 3rd). Applying two algorithms in sequence, first either CALM or TSPCA, followed by MEG Denoise, also resulted in a large increase in broadband SNR (Figure 12A, columns 6 and 7). For all three stimulus conditions, the combination of MEG Denoise and CALM resulted in the largest gain in SNR, significantly larger than MEG Denoise alone for two out of the three conditions (Figure 12B, 5th versus 4th bars). This indicates that the MEG Denoise algorithm and an environmental algorithm captured some independent noise.

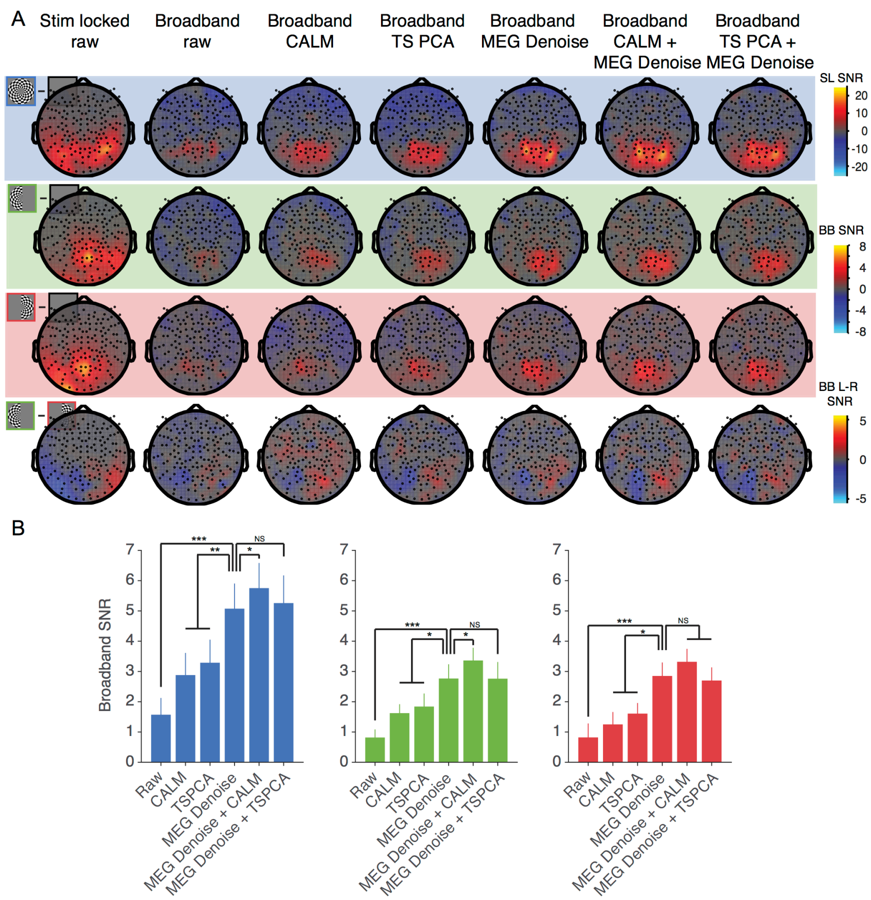

Figure 12. Comparison of different denoising algorithms on NYU datasets (averaged across subjects S1-S8). (A) The columns represent SNR values for the stimulus locked signal (column 1), broadband signal without denoising (column 2), and broadband signal with one or more denoising algorithms. One scale bar is used for all stimulus locked plots (column 1). A second scale bar is used for all broadband plots (columns 2-7) except for the Left minus Right plots (row 4, columns 2-7). Other details as in Figure 5. (B) Broadband SNR using different algorithms for both-hemifield (left), left-hemifield (center) and right-hemifield (right) stimuli. Each bar is the change in SNR from baseline (column 2 in panel A), averaged across the top 10 sensors per subject (mean +/- SEM across subjects). Top sensors were defined as the 10

sensors from each subject with the highest SNR across any of the 3 stimulus conditions and any of the denoising algorithms (columns 2-7). Statistical significance computed and indicated as in Figure 11. Made with *dfdMakeFigure12.m*.

Effect of denoising on stimulus locked SNR

In a separate analysis, we ran the MEG Denoise algorithm to evaluate its effect on the stimulus locked signal. The methods were identical to those used to denoise the broadband signal except for the omission of one step, the step in which we filtered the time series to remove temporal components that do not contribute to the broadband signal. Denoising modestly increased the stimulus-locked SNR for all stimulus conditions for most subjects (Figure 13, top). The SNR increased numerically in all subjects (n=8) and in all stimulus conditions, although the percentage increases were smaller than those for denoising the broadband signal, ~20% increase compared to two-fold. As in the case of denoising the broadband signals, the main contribution to the increase in SNR for the stimulus-locked signal was a decrease in variability across epochs (Figure 13, bottom), rather than an increase in the signal level (Figure 13, middle).

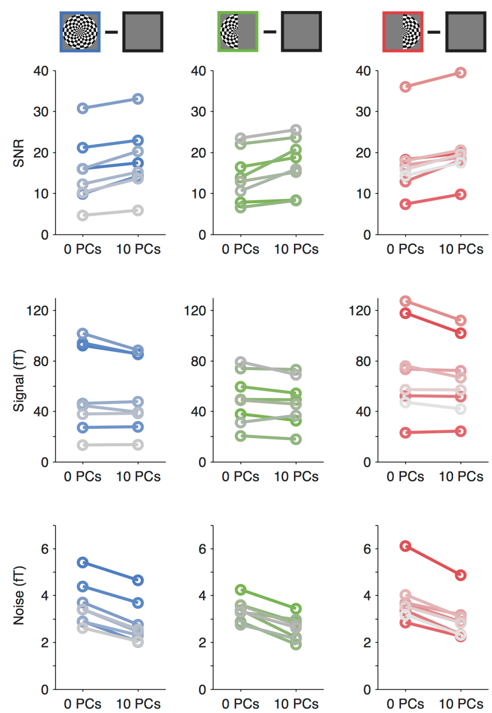

Figure 13. Denoising the stimulus-locked signal. The MEG Denoise algorithm results in a modest increase in SNR for most subjects in all three stimulus conditions (top row). This benefit is largely due to the fact that the noise level goes down from denoising (middle bottom) rather than the signal increasing (middle row). Plotting conventions as in Figure 7c and Figure 8. Made with *dfdMakeFigure13.m*.

Broadband fields measured with Elekta 360 Neuromag

To test whether the findings reported above generalize to other instruments and experimental environments, we conducted the same experiment using a different type of MEG system, an Elekta 360 Neuromag at CiNet. The CiNet system contains paired planar gradiometers, in contrast to the axial gradiometers used in the Yokogawa MEG at NYU, and the scanner is situated in a different physical environment, with potentially very different sources of environmental noise. The pre-processing pipeline at this imaging center often includes a denoising step based on temporally extended signal source separation (tSSS) (Taulu and Simola, 2006; Taulu and Hari, 2009). This additional experiment gave us the opportunity to ask several questions: (1) Are broadband fields observed with a different MEG sensor type and different physical environment? (2) Does the tSSS algorithm increase the broadband SNR? (3) Does our new MEG Denoise algorithm increase the SNR of data that have already been denoised with the tSSS algorithm?

The identical experiments were conducted with 4 new subjects. As expected, all three stimulus types led to a large stimulus-locked response in the posterior sensors, with a peak SNR of more than 10 in the group averaged data (Figure 14A, column 1). A modest, spatially specific broadband signal was measured from the undenoised data for each stimulus type (Figure 14A column 2), with a peak SNR of 1-2 in the group-average data for all three conditions. Unlike the NYU data, in the CiNet data the MEG Denoise algorithm on the raw data did not generally result in an increase in the broadband SNR (group data, Figure 14A, columns 2 and 3; individual subjects, Figure 14B, left side of each subplot). However, when the raw data were pre-processed with the tSSS algorithm (Figure 14A, column 4), application of MEG Denoise increased the SNR in all 3 stimulus conditions for 3 out of 4 subjects, and in 2 out of 3 stimulus conditions for the 4th subject. Together, the MEG Denoise algorithm increased the SNR by 2-3 fold, similar to the NYU data (both-hemifield: 2.8 to 5.6; left-hemifield: 0.8 to 2.4; right-hemifield: 2.01 to 4.4; means across subjects 1-4, top 10 sensors each, for the tSSS data and the MEG Denoised tSSS data). Just as with the NYU MEG data set, the combination of an algorithm tailored to find environmental noise (tSSS) and our algorithm produced the most robust results, indicating that MEG-denoise and the environmental denoising algorithm removed at least some independent sources of noise.

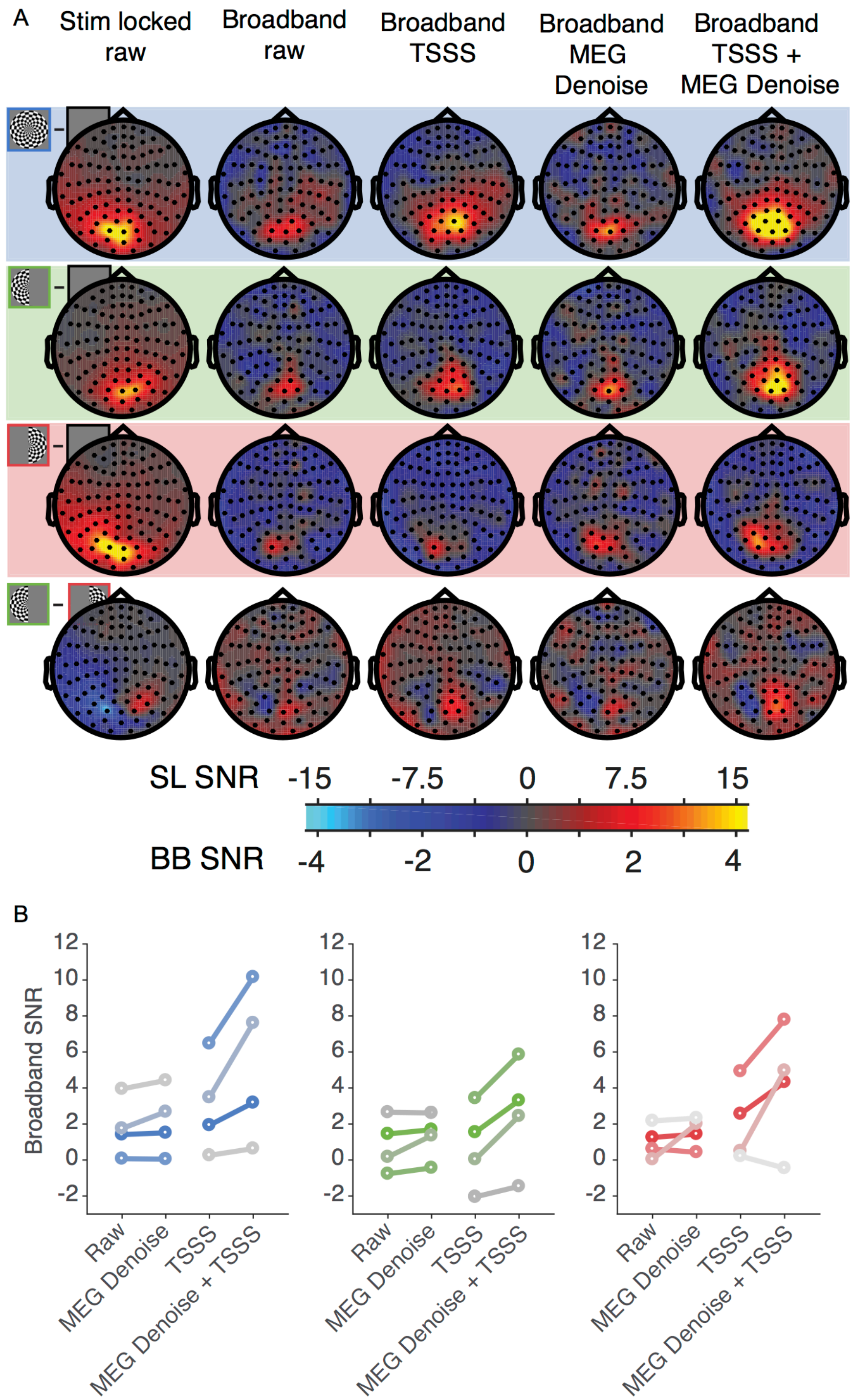

Figure 14. MEG data from CiNet Neuromag. (A) All plots show data averaged across new 4 subjects (S9-S13) in sensor space (sensor-wise mean of the subject SNR). The columns represent SNR values for the stimulus locked signal (column 1), broadband signal without denoising (column 2), and broadband signal with one or more denoising algorithms. The same scale bar is used for all broadband data (columns 3 - 5). Other details as in Figure 5. (B) Broadband SNR using different algorithms for both-hemifield (left), left-hemifield (center) and right-hemifield (right) stimuli. Each line is average broadband SNR across the top 10 sensors for one individual. Top sensors were defined as the 10 sensors from each subject with the highest SNR across any of the 3 stimulus conditions and any of the denoising algorithms (columns 2-6). Made with *dfdMakeFigure14.m*.

Saccadic eye movements during MEG experiments

Saccadic eye movements are known to have a large influence on MEG and EEG measurements. This influence can be especially pernicious when measuring high frequency broadband signals, because the spike field (MEG) or spike potential (EEG) arising from extraocular muscle contraction can be spectrally broadband and can co-vary with task design; hence, it can easily be confused with broadband signals arising from brain activity (Yuval-Greenberg et al., 2008; Yuval-Greenberg and Deouell, 2009). For visual experiments, the spike potential in EEG is especially problematic because it tends to affect sensors which are also visually sensitive (posterior middle). In contrast, the MEG spike field is lateral, potentially influencing temporal and frontal sensors, with little to no effect on posterior sensors (Carl et al., 2012). Hence spike field artifacts are unlikely to contaminate our visually elicited broadband signals, which are most clearly evident in the central posterior sensors.

Nonetheless, for a subset of subjects (S6-S8), we measured eye movements during the MEG experiments and quantified the frequency of microsaccades, and the distribution of microsaccade direction, for each stimulus condition. Each of these 3 subjects showed broadband responses in their denoised data (Figure 10). All three subjects showed a higher rate of horizontal than vertical microsaccades in every stimulus condition (Figure 15), consistent with prior observations (Engbert, 2006), but there was no systematic pattern in saccade frequency as a function of stimulus condition; for example, the stimulus condition with the most and with the fewest microsaccades differed across the 3 subjects. Moreover, the subject with the highest broadband SNR among these 3 (S6) had the lowest rate of microsaccades (~0.5 microsaccades / second). To test more directly whether microsaccades contributed to the measured broadband fields, we re-analyzed the data from these 3 subjects in two ways, either limited to only those epochs with microsaccades or only those epochs without microsaccades (Figure 15b). The broadband responses were evident in each subject in the epochs without microsaccades, indicating that this response is not entirely an artifact of microsaccades.

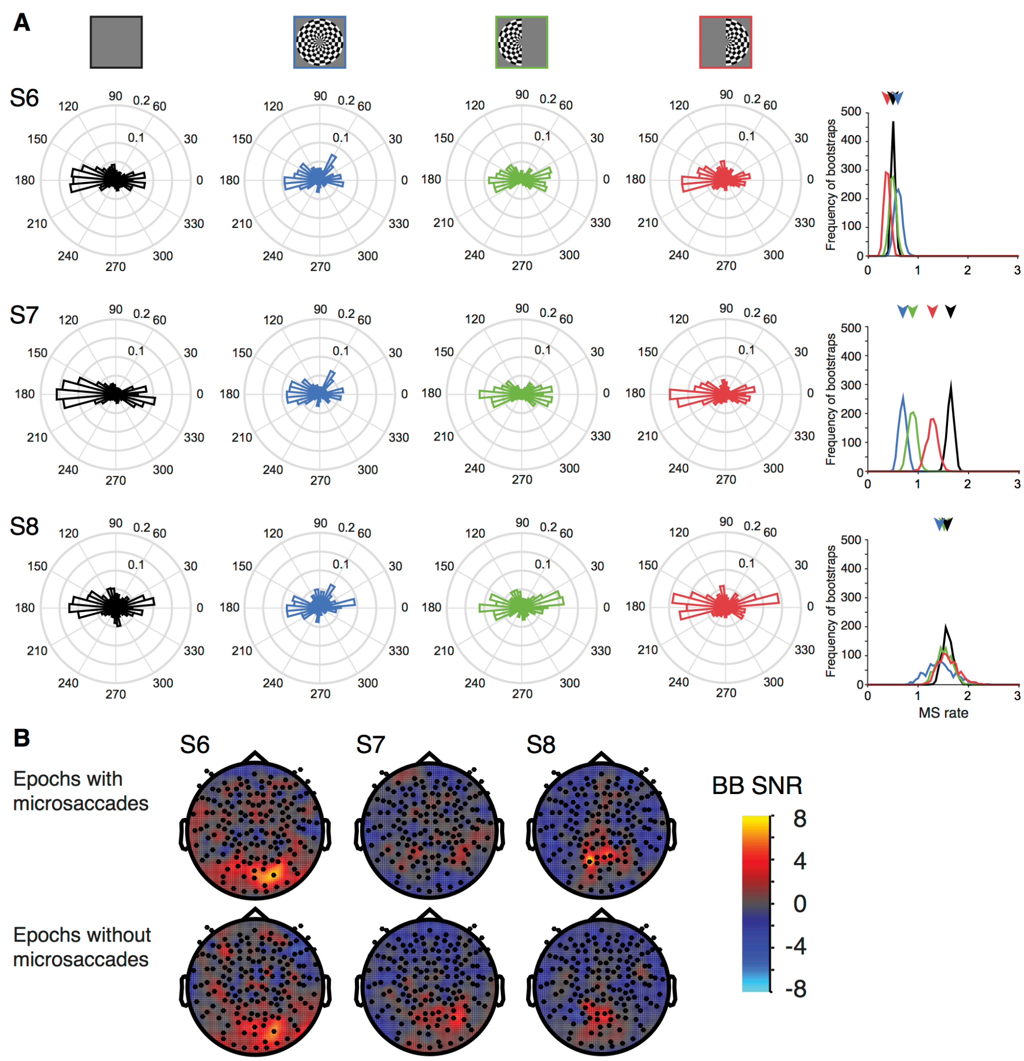

Figure 15. Microsaccades during experimental conditions. (A) The circular histograms show the frequency of microsaccades per 1-s epoch, binned by direction, for each of the 4 stimulus conditions (columns 1-4). The rows show data for 3 subjects. The last column shows the rate of microsaccades (per 1-s epoch) irrespective of direction, for each of the 4 stimulus conditions, bootstrapped 100 times over epochs. Arrows indicate the median rate for each condition. (B) Both-hemifield minus blank broadband SNR meshes limited to only those epochs with microsaccades (top row) or without microsaccades (bottom row). Made with *dfdMakeFigure15.m*.

Discussion

Summary

We separated the MEG signal into two components, one time-locked and one asynchronous with the stimulus. The stimulus-locked component, quantified by the amplitude at the contrast reversal frequency (12 Hz), was clearly visible in all subjects with minimal preprocessing. The signal showed spatial specificity, in that it was observed in occipital sensors, with higher SNR contralateral to the lateralized stimuli. These results are consistent with a long literature of steady state evoked potentials and fields, measured extracranially (Adrian and Matthews, 1934a; Norcia et al., 2015) and intracranially (Winawer et al., 2013).

The asynchronous signal, spanning a broad range of frequencies (60-150 Hz), was visible with little preprocessing in some subjects and in the mean across subjects. However, this broadband response had low SNR compared to the stimulus-locked component. With our new automated denoising algorithm, the broadband SNR increased more than 2-fold, such that we could obtain reliable, spatially specific broadband signals in all individual observers. We showed in a subset of subjects that the broadband signals could not be explained by systematic biases in the pattern of fixational eye movements, supporting the interpretation that the broadband fields arise from neural activity and not from artifacts associated with eye movements. Finally, we showed that we obtained similar results using two different MEG instruments, a Yokogawa MEG with 157 axial gradiometers (NYU), and an Elekta 360 with 204 paired planar gradiometers (CiNet).

These results are *qualitatively* consistent with intracranial measurements in human using a similar stimulus paradigm (Winawer et al., 2013). However, it has proven much more difficult in the past to measure extracranial broadband signals arising from neural activity, in part because the extracranial signals are small. Below, we discuss the significance of broadband responses, challenges in measuring them extracranially, and the generalizability of our denoising algorithm.

Significance of broadband responses

In the 1920s and 30s, Hans Berger and others described oscillatory signals in surface EEG between 10 and 25 Hz (Berger, 1929; Adrian and Matthews, 1934b). Narrow peaks in EEG and MEG spectra have served as useful indices of cognitive, motor, and sensory engagement, and have been interpreted as a measure of coherence within a neuronal population. More recently, using intracranial recordings from patients, Crone and colleagues (1998) described an increase in power in higher frequencies (75-100 Hz) associated with motor movements. Subsequently, this high frequency power elevation was interpreted as a broadband (not oscillatory) signal, thought to reflect an increased level of activity within individual neurons, rather than an increase in neuronal synchrony (Miller et al., 2007; Miller et al., 2009b; Miller et al., 2009c). In support of this interpretation, it has been found that the level of the broadband signal correlates with single (Manning et al., 2009) and multiunit spike rates (Ray and Maunsell, 2011). Under some conditions, it is also correlated with the fMRI BOLD signal (Hermes et al., 2012b; Winawer et al., 2013). The BOLD signal, however, is influenced by processes other than spiking (Mathiesen et al., 1998; Logothetis and Wandell, 2004; Sirotin and Das, 2009); hence quantifying broadband responses from the same stimuli or conditions studied with fMRI can help disentangle the relative contribution of spiking versus other, non-spiking neural activity, to an observed BOLD response. Moreover, ECoG studies in many different parts of the brain have measured broadband power elevations associated with perception, movement, language, and cognition (Crone et al., 2006; Miller et al., 2009a; Hermes et al., 2012a; Miller et al., 2014) (Figure 16). Being able to reliably measure the broadband signal extracranially offers the opportunity to infer the level of neuronal responses noninvasively and at a sub-second scale, complementing fMRI, as well as the oscillatory and time-locked (evoked) signals more commonly made with MEG and EEG.

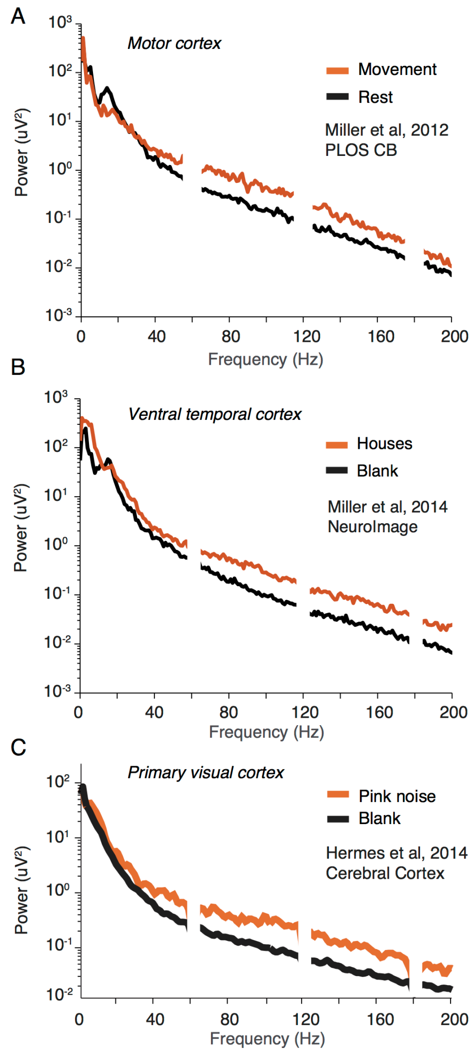

Figure 16. Broadband signals around the brain. Examples of broadband field potentials from single ECoG electrodes in motor cortex (top), ventral temporal cortex (middle), and primary visual cortex (bottom). The power increases relative to baseline span at least 50 to 200 Hz. Adapted from (A) (Miller et al., 2012); (B) (Miller et al., 2014); (C) (Hermes et al., 2015).

Relation to prior measures of extracranial broadband and gamma band responses

Broadband vs. narrowband gamma. Several groups have distinguished between broadband power increases and narrowband gamma oscillations (Henrie and Shapley, 2005; Ray and Maunsell, 2011; Miller et al., 2014). The narrowband oscillation is reliably observed in visual cortex for some stimuli (e.g., high contrast bars and gratings) (Kayser et al., 2003; Jia et al., 2011; Miller et al., 2014). It typically has a peak frequency between 30 and 100 Hz and a bandwidth of ~10-20 Hz. The broadband response, in contrast, is found in many brain areas and for many types of stimuli, and spans at least 50-150 Hz, but can also extend to lower and higher frequencies (Miller et al., 2009c; Winawer et al., 2013). Robust narrowband gamma oscillations have been measured using MEG. For example, Hoogenboom et al (2006), using grating stimuli, measured a large signal peaked between 60 and 80 Hz with a bandwidth of about 10 Hz. Similar responses have been measured by other groups, most often with MEG but also with EEG (Muthukumaraswamy and Singh, 2013). These narrowband oscillations are quite different from the broadband fields we measured here, which span a much wider frequency range, have a lower amplitude, and likely reflect asynchronous neural activity rather than oscillations.

Multiple gamma peaks. Some extracranial studies have reported multiple distinct signals within the gamma band in a single experiment. For example, Wyart and Tallon-Baudry (2008) and Vidal et. al. (2006) measured MEG responses to gratings and bars, respectively. They reported increases in power spanning 40-120 Hz, and interpreted this as two narrowband peaks, one between 45 and 65 Hz and the other between 75 and 120 Hz. Both components were interpreted as oscillations arising from synchronous neural activity, and are likely different from the broadband signals we report here.

Group averaged broadband. Two MEG studies reported increases in high gamma power (60-140 Hz) during recall of visual stimuli (Nieuwenhuis et al., 2008; Nieuwenhuis et al., 2012). These studies showed the average across subjects (22 or 24), so that it is not known whether there were reliable responses in each separate subject.

Motor cortex. High frequency spectral power elevation (~65-100 Hz) has been shown from motor cortex measured extracranially (Ball et al., 2008; Darvas et al., 2010). This signal was most evident in group-averaged data and some but not all individuals, and were most reliable within a relative narrow band (~20-30 Hz wide). Ball *et al.* (2008) noted that better methods for measuring high frequency broadband extracranially would help resolve whether individual differences were due to measurement limitations or to the lack of high frequency brain signals in some subjects. Cheyne *et al.* (2008) measured high gamma (65-80 Hz) with MEG over motor cortex in individual subjects, and speculated that these signals reflect cortico-basal ganglia loops, as the subthalamic nucleus in the basal ganglia is known to have narrowband oscillations peaked at 70-80 Hz.

Challenges in measuring extracranial broadband responses

Extracranial broadband signal strength is low. Although having a high SNR after denoising, the MEG broadband signal was nonetheless small relative to baseline – about a 13% increase. Using nearly the identical stimulus, the broadband signal measured by ECoG was about 15 times larger (2.9 fold, or a ~190% increase over baseline) (Winawer et al., 2013). In contrast, the discrepancy was much smaller for the stimulus locked signal (an almost 8-fold increase over baseline measured with MEG, and 21-fold with ECoG). Why are the MEG broadband signals small? First, the MEG sensors pool over a large area, so that the baseline power reflects activity from a large fraction of the brain, whereas the visually driven broadband response likely comes from a much smaller region of cortex (Krusienski et al., 2011). In contrast, both the baseline and visually driven responses in an ECoG electrode on visual cortex arise from the same patch of brain tissue. Second, the signal amplitude depends not only on the pooling area, but also the phase coherence. If the broadband signal arises from incoherent neural activity, and the stimulus locked signal arises from coherent (synchronous) neural activity, then the former will grow with the square root of the number of the sources, and the latter with the number of sources. Since MEG pools over a much larger region of cortex than ECoG, the ratio of incoherent signal strength (e.g. broadband) to coherent (e.g. stimulus-locked) will be much lower. This logic is supported by modeling studies (Linden et al., 2011) and empirical studies with intra- and extracranial measures, which found that the signals which were more coherent intracranially had the highest efficiency in transmission to outside the head (Pfurtscheller and Cooper, 1975; Dalal et al., 2009).

Extracranial measurements contain multiple noise sources. Because the extracranial broadband power is low, noise becomes a potentially major impediment. Fixational eye movements (Yuval-Greenberg et al., 2008), head muscle contraction (Muthukumaraswamy, 2013), and environmental perturbations (Hämäläinen et al., 1993), produce noise picked up by MEG and EEG sensors, in addition to the intrinsic noise from the brain (Gonen-Yaacovi et al., 2016). Many of these noise sources are spectrally broad and hence particularly problematic when investigating neural broadband signals.

Although spike fields generated from eye movements can be mistaken for broadband neural activity (sometimes called a "gamma imposter"; (Yuval-Greenberg and Deouell, 2009)), it is unlikely that our spatially-specific broadband measures were substantially contaminated by eye movement artifacts. This was confirmed by our analyses of eye movement data in a subset of subjects, and by the fact that the middle posterior sensors where we observed broadband are not usually associated with MEG spike field artifacts (Carl et al., 2012). A second confound from eye movements, the electromagnetic fields arising from movement of the retina-to-cornea dipole, causes low frequency artifacts (4-20 Hz; (Keren et al., 2010), table 1) and therefore is unlikely to have affected our broadband measures (60-150 Hz).

Head muscles, like extraocular muscles, can also give rise to spectrally broadband contaminants (Muthukumaraswamy, 2013), as can many sources of noise outside the subject, from nearby subways to MRI centers to electrical equipment. Many of these sources could cause broadband signals. However, all of these noise sources are unlikely to be confined to occipital sensors and to co-vary with stimulus condition, and hence do not explain our broadband observations. Moreover, it is likely that these noise sources, if present, were included in our noise pool, and hence MEG Denoise would have reduced the effect of these large-scale noise artifacts.

MEG Denoise and other denoising algorithm

The MEG Denoise algorithm we present uses principal component analysis on a subset of sensors to remove noise. In principle, it can capture any noise source that contributes to the noise pool, including environmental, oculomotor, muscular, and neural. This differs from algorithms such as CALM, TSPCA, and tSSS, which are explicitly designed to remove environmental noise. Hence MEG Denoise is complementary to these methods. We found that the most effective analysis sequence was either to use MEG Denoise alone on the minimally pre-processed data, or to use an environmental denoising algorithm as a pre-processing step prior to running MEG Denoise. The algorithm has much in common with ICA denoising (Vigario, 1997), with a few important differences. First, PCA, unlike ICA, ranks the components by variance explained. Second, MEG Denoise explicitly separates the sensors into a noise pool and a potential signal pool. The combination of these features makes it easy to automate which components to project out. A benefit of automaticity is that it is easy to perform PCA, and hence denoise the data, at the time scale of individual events (e.g., >1,000 one-second epochs here). If the spatial pattern (the weights) of the PCs vary over time, then deriving the components independently within short epochs may be more effective, as demonstrated here (Figure 11, bars 1 versus 2).

To use MEG Denoise for other experimental designs, analyses, or scanners, one would need to change some of the input parameters. In particular, in addition to the experimental design matrix and data, there are two required inputs. These are the experiment-specific functions to summarize the MEG responses. In our experiments, one function computed the stimulus-locked signal and was used to define the noise pool. For most of our analyses, the other function computed the broadband power, which was the dependent measure. In principle, one could use a single function to both define the noise pool and evaluate the data, and in fact this is what we did when we denoised the stimulus-locked signal. For other experiments, one might use a function that computes the amplitude or latency of an evoked response, or the power in a limited temporal frequency band, or any measure relevant to the experiment. Alternatively, one could run a separate localizer experiment to identify a pool of potential sensors of interest and a pool of noise sensors, and then manually enter the list of noise sensors to denoise the main experiment. There are a number of other optional inputs, such as the method to identify the noise pool, the accuracy metric (SNR / R^2). For this paper, we used the defaults for all optional inputs.

Conclusion

We designed an experiment to elicit spatially specific patterns of MEG sensor responses and we developed a new denoising algorithm for MEG data. The results show that stimulus-driven broadband brain responses can be quantitatively characterized in individual subjects using a non-invasive method. Because we obtain high SNR measures from short experiments, the broadband signal can be used to address a wide range of scientific questions. Having access to this signal opens a window for neuroscientists to study signals associated with neuronal spike rates non-invasively at a high temporal resolution in the living human brain.

Notes

Supplementary material for this article will be made available online. This material has not been peer reviewed.

References

Adachi Y, Shimogawara M, Higuchi M, Haruta Y, Ochiai M (2001) Reduction of non-periodic environmental magnetic noise in MEG measurement by continuously adjusted least squares method. Ieee T Appl Supercon 11:669-672.

Adrian ED, Matthews BHC (1934a) The Berger rhythm potential changes from the occipital lobes in man. Brain 57:355-385.

Adrian ED, Matthews BH (1934b) The interpretation of potential waves in the cortex. J Physiol 81:440-471.

Ball T, Demandt E, Mutschler I, Neitzel E, Mehring C, Vogt K, Aertsen A, Schulze-Bonhage A (2008) Movement related activity in the high gamma range of the human EEG. Neuroimage 41:302-310.

Berger H (1929) Über Elektroenkephalogramm des Menschen. European Archives of Psychiatry and Clinical Neuroscience 87:527-570.

Brainard DH (1997) The Psychophysics Toolbox. Spat Vis 10:433-436.

Buzsaki G, Anastassiou CA, Koch C (2012) The origin of extracellular fields and currents--EEG, ECoG, LFP and spikes. Nature reviews Neuroscience 13:407-420.

Carl C, Acik A, Konig P, Engel AK, Hipp JF (2012) The saccadic spike artifact in MEG. Neuroimage 59:1657-1667.

Cheyne D, Bells S, Ferrari P, Gaetz W, Bostan AC (2008) Self-paced movements induce high-frequency gamma oscillations in primary motor cortex. Neuroimage 42:332-342.

Crone NE, Sinai A, Korzeniewska A (2006) High-frequency gamma oscillations and human brain mapping with electrocorticography. 159:275-295.

Crone NE, Miglioretti DL, Gordon B, Lesser RP (1998) Functional mapping of human sensorimotor cortex with electrocorticographic spectral analysis. II. Event-related synchronization in the gamma band. Brain 121 (Pt 12):2301-2315.

Dalal SS, Baillet S, Adam C, Ducorps A, Schwartz D, Jerbi K, Bertrand O, Garnero L, Martinerie J, Lachaux JP (2009) Simultaneous MEG and intracranial EEG recordings during attentive reading. Neuroimage 45:1289-1304.

Darvas F, Scherer R, Ojemann JG, Rao RP, Miller KJ, Sorensen LB (2010) High gamma mapping using EEG. Neuroimage 49:930-938.

de Cheveigne A, Simon JZ (2007) Denoising based on time-shift PCA. Journal of neuroscience methods 165:297-305.

Engbert R (2006) Microsaccades: A microcosm for research on oculomotor control, attention, and visual perception. Prog Brain Res 154:177-192.

Engbert R, Mergenthaler K (2006) Microsaccades are triggered by low retinal image slip. Proc Natl Acad Sci U S A 103:7192-7197.

Fries P, Scheeringa R, Oostenveld R (2008) Finding gamma. Neuron 58:303-305.

Gonen-Yaacovi G, Arazi A, Shahar N, Karmon A, Haar S, Meiran N, Dinstein I (2016) Increased ongoing neural variability in ADHD. Cortex 81:50-63.

Hämäläinen M, Hari R, Ilmoniemi RJ, Knuutila J, Lounasmaa OV (1993) Magnetoencephalography—theory, instrumentation, and applications to noninvasive studies of the working human brain. Reviews of modern Physics 65:413.

Harvey BM, Vansteensel MJ, Ferrier CH, Petridou N, Zuiderbaan W, Aarnoutse EJ, Bleichner MG, Dijkerman HC, van Zandvoort MJ, Leijten FS, Ramsey NF, Dumoulin SO (2013) Frequency specific spatial interactions in human electrocorticography: V1 alpha oscillations reflect surround suppression. Neuroimage 65:424-432.

Henrie JA, Shapley R (2005) LFP power spectra in V1 cortex: the graded effect of stimulus contrast. Journal of neurophysiology 94:479-490.

Hermes D, Miller KJ, Wandell BA, Winawer J (2015) Stimulus Dependence of Gamma Oscillations in Human Visual Cortex. Cerebral cortex 25:2951-2959.

Hermes D, Siero JC, Aarnoutse EJ, Leijten FS, Petridou N, Ramsey NF (2012a) Dissociation between neuronal activity in sensorimotor cortex and hand movement revealed as a function of movement rate. J Neurosci 32:9736-9744.

Hermes D, Miller KJ, Vansteensel MJ, Aarnoutse EJ, Leijten FS, Ramsey NF (2012b) Neurophysiologic correlates of fMRI in human motor cortex. Human brain mapping 33:1689-1699.

Honey CJ, Thesen T, Donner TH, Silbert LJ, Carlson CE, Devinsky O, Doyle WK, Rubin N, Heeger DJ, Hasson U (2012) Slow cortical dynamics and the accumulation of information over long timescales. Neuron 76:423-434.

Hoogenboom N, Schoffelen JM, Oostenveld R, Parkes LM, Fries P (2006) Localizing human visual gamma-band activity in frequency, time and space. NeuroImage 29:764-773.

Jia X, Smith MA, Kohn A (2011) Stimulus selectivity and spatial coherence of gamma components of the local field potential. J Neurosci 31:9390-9403.

Kay KN, Rokem A, Winawer J, Dougherty RF, Wandell BA (2013) GLMdenoise: a fast, automated technique for denoising task-based fMRI data. Frontiers in neuroscience 7:247.

Kayser C, Salazar RF, Konig P (2003) Responses to natural scenes in cat V1. Journal of neurophysiology 90:1910-1920.

Keren AS, Yuval-Greenberg S, Deouell LY (2010) Saccadic spike potentials in gamma-band EEG: characterization, detection and suppression. Neuroimage 49:2248-2263.

Krusienski DJ, Grosse-Wentrup M, Galan F, Coyle D, Miller KJ, Forney E, Anderson CW (2011) Critical issues in state-of-the-art brain-computer interface signal processing. J Neural Eng 8:025002.

Lima B, Cardoso MM, Sirotin YB, Das A (2014) Stimulus-related neuroimaging in task-engaged subjects is best predicted by concurrent spiking. J Neurosci 34:13878-13891.

Linden H, Tetzlaff T, Potjans TC, Pettersen KH, Grun S, Diesmann M, Einevoll GT (2011) Modeling the spatial reach of the LFP. Neuron 72:859-872.

Liu J, Newsome WT (2006) Local field potential in cortical area MT: stimulus tuning and behavioral correlations. J Neurosci 26:7779-7790.

Logothetis NK, Wandell BA (2004) Interpreting the BOLD signal. Annu Rev Physiol 66:735-769.

Manning JR, Jacobs J, Fried I, Kahana MJ (2009) Broadband shifts in local field potential power spectra are correlated with single-neuron spiking in humans. J Neurosci 29:13613-13620.

Mathiesen C, Caesar K, Akgoren N, Lauritzen M (1998) Modification of activity-dependent increases of cerebral blood flow by excitatory synaptic activity and spikes in rat cerebellar cortex. J Physiol 512 (Pt 2):555-566.

Miller KJ, Weaver KE, Ojemann JG (2009a) Direct electrophysiological measurement of human default network areas. Proc Natl Acad Sci U S A 106:12174-12177.

Miller KJ, Sorensen LB, Ojemann JG, den Nijs M (2009b) Power-law scaling in the brain surface electric potential. PLoS computational biology 5:e1000609.

Miller KJ, Zanos S, Fetz EE, den Nijs M, Ojemann JG (2009c) Decoupling the cortical power spectrum reveals real-time representation of individual finger movements in humans. J Neurosci 29:3132-3137.

Miller KJ, Honey CJ, Hermes D, Rao RP, denNijs M, Ojemann JG (2014) Broadband changes in the cortical surface potential track activation of functionally diverse neuronal populations. Neuroimage 85 Pt 2:711-720.

Miller KJ, Leuthardt EC, Schalk G, Rao RP, Anderson NR, Moran DW, Miller JW, Ojemann JG (2007) Spectral changes in cortical surface potentials during motor movement. J Neurosci 27:2424-2432.

Miller KJ, Hermes D, Honey CJ, Hebb AO, Ramsey NF, Knight RT, Ojemann JG, Fetz EE (2012) Human motor cortical activity is selectively phase-entrained on underlying rhythms. PLoS Comput Biol 8:e1002655.

Muthukumaraswamy SD (2013) High-frequency brain activity and muscle artifacts in MEG/EEG: a review and recommendations. Front Hum Neurosci 7:138.

Muthukumaraswamy SD, Singh KD (2013) Visual gamma oscillations: the effects of stimulus type, visual field coverage and stimulus motion on MEG and EEG recordings. Neuroimage 69:223-230.

Nieuwenhuis IL, Takashima A, Oostenveld R, Fernandez G, Jensen O (2008) Visual areas become less engaged in associative recall following memory stabilization. Neuroimage 40:1319-1327.

Nieuwenhuis IL, Takashima A, Oostenveld R, McNaughton BL, Fernandez G, Jensen O (2012) The neocortical network representing associative memory reorganizes with time in a process engaging the anterior temporal lobe. Cereb Cortex 22:2622-2633.

Norcia AM, Appelbaum LG, Ales JM, Cottereau BR, Rossion B (2015) The steady-state visual evoked potential in vision research: A review. J Vis 15:4.

Oostenveld R, Fries P, Maris E, Schoffelen JM (2011) FieldTrip: Open source software for advanced analysis of MEG, EEG, and invasive electrophysiological data. Computational intelligence and neuroscience 2011:156869.

Pelli DG (1997) The VideoToolbox software for visual psychophysics: transforming numbers into movies. Spat Vis 10:437-442.

Pfurtscheller G, Cooper R (1975) Frequency dependence of the transmission of the EEG from cortex to scalp. Electroencephalography and clinical neurophysiology 38:93-96.

Podvalny E, Yeagle E, Megevand P, Sarid N, Harel M, Chechik G, Mehta AD, Malach R (2017) Invariant Temporal Dynamics Underlie Perceptual Stability in Human Visual Cortex. Curr Biol 27:155-165.

Ray S, Maunsell JH (2011) Different origins of gamma rhythm and high-gamma activity in macaque visual cortex. PLoS biology 9:e1000610.

Schalk G, Leuthardt EC (2011) Brain-computer interfaces using electrocorticographic signals. IEEE Rev Biomed Eng 4:140-154.

Seki K, Nakasato N, Fujita S, Hatanaka K, Kawamura T, Kanno A, Yoshimoto T (1996) Neuromagnetic evidence that the P100 component of the pattern reversal visual evoked response originates in the bottom of the calcarine fissure. Electroencephalography and clinical neurophysiology 100:436-442.

Sirotin YB, Das A (2009) Anticipatory haemodynamic signals in sensory cortex not predicted by local neuronal activity. Nature 457:475-479.

Taulu S, Simola J (2006) Spatiotemporal signal space separation method for rejecting nearby interference in MEG measurements. Phys Med Biol 51:1759-1768.

Taulu S, Hari R (2009) Removal of magnetoencephalographic artifacts with temporal signal-space separation: demonstration with single-trial auditory-evoked responses. Hum Brain Mapp 30:1524-1534.

Vidal JR, Chaumon M, O'Regan JK, Tallon-Baudry C (2006) Visual grouping and the focusing of attention induce gamma-band oscillations at different frequencies in human magnetoencephalogram signals. J Cogn Neurosci 18:1850-1862.

Vigario RN (1997) Extraction of ocular artefacts from EEG using independent component analysis. Electroen Clin Neuro 103:395-404.

Winawer J, Kay KN, Foster BL, Rauschecker AM, Parvizi J, Wandell BA (2013) Asynchronous broadband signals are the principal source of the BOLD response in human visual cortex. Curr Biol 23:1145-1153.

Wyart V, Tallon-Baudry C (2008) Neural dissociation between visual awareness and spatial attention. J Neurosci 28:2667-2679.

Yuval-Greenberg S, Deouell LY (2009) The broadband-transient induced gamma-band response in scalp EEG reflects the execution of saccades. Brain Topogr 22:3-6.

Yuval-Greenberg S, Deouell LY (2011) Scalp-recorded induced gamma-band responses to auditory stimulation and its correlations with saccadic muscle-activity. Brain Topogr 24:30-39.

Yuval-Greenberg S, Tomer O, Keren AS, Nelken I, Deouell LY (2008) Transient induced gamma-band response in EEG as a manifestation of miniature saccades. Neuron 58:429-441.